Journal of Polymer Science

WILEY

JOURNAL OF POLYMER SCIENCE

RESEARCH ARTICLE OPEN ACCESS

Kinetics of ε-Caprolactone Ring Opening Polymerization: Experimental and Modeling Study

Jakub Staś[1,2] | Milan Den Haese[3] | Luca Cannas[4] | Anton Ginzburg[4] | Louis Pitet[3] | Bart Van der Bruggen[2,5,6] | Alexandr Zubov[1]

[1]Department of Chemical Engineering, University of Chemistry and Technology Prague, Prague, Czech Republic | [2]Department of Chemical Engineering, Process Engineering for Sustainable Systems (ProcESS), KU Leuven, Leuven, Belgium | [3]Advanced Functional Polymers Laboratory, Institute for Materials Research (Imo-Imomec), Hasselt University, Hasselt, Belgium | [4]Department of Chemical Engineering, KU Leuven, Diepenbeek, Belgium | [5]Department of Chemical and Biochemical Engineering, Korea University, Seoul, Republic of Korea | [6]Nanotechnology Centre, CEET, VSB-Technical University of Ostrava, Ostrava-Poruba, Czech Republic

Correspondence: Alexandr Zubov (alexandr.zubov@vscht.cz)

Received: 30 March 2026 | **Revised:** 6 May 2026 | **Accepted:** 14 May 2026

Keywords: kinetic parameters | polycaprolactone | polymerization mechanism | ring-opening polymerization | stannous octoate | ε-caprolactone

ABSTRACT

Although polycaprolactone (PCL) is an established biodegradable polymer with various applications, comprehensive kinetic modeling of its production is very rare. We present a multi-scale model of ring-opening polymerization (ROP) of ε-caprolactone catalyzed by tin(II) octoate as a standard industrial method of PCL production. Five batch polymerization experiments with varying temperature and monomer/initiator ratio were conducted, leading to the production of linear PCL samples of varying molecular weight distributions. The experimental data were subsequently used for the rigorous estimation of kinetic parameters associated with the elementary reaction steps in the assumed kinetic scheme. The results of the model predictions are compared with experimental data with decent agreement, revealing that although the reaction dynamics are significantly slower for ROP of ε-caprolactone than for L,L-lactide, the original kinetic scheme previously validated for polylactide production can be successfully used to model the PCL production process.

1 | Introduction

Currently, there are trends around the world to substitute conventional polymers with biodegradable ones, such as polycaprolactone (PCL). PCL is a polymer that was first synthesized in the early 1930s and is still of promising use today [1]. Its main advantages are its biodegradability and biocompatibility. This means that PCL is decomposed through biological processes and that the substances that form during this process are not harmful to organisms and tissues. Thanks to these properties, PCL is used separately or as a copolymer with other biopolymers, such as drug delivery systems, to produce sutures [1–6] or as scaffolds in tissue engineering (bones, cartilage, tendons, ligaments, blood vessels, skin, nerves, and others) [7–13]. PCL is widely used in tissue engineering thanks to its relatively low cost, high processing capacity, and ability to maintain structural rigidity in physiological environments [14].

For industrial applications, it is useful to know the kinetics of polymerization and the change in product chain length distribution to synthesize polymers with desired properties or optimize the production process [15, 16]. A widely used method of industrial PCL production is ring-opening polymerization (ROP) of caprolactone, catalyzed by stannous octoate, $Sn(Oct)_2$, usually with alcohol as an initiator [17–19]. The mechanism of caprolactone ROP catalyzed by $Sn(Oct)_2$ bears many similarities with ROP of L,L-lactide, proceeding via the same coordination-insertion mechanism [20–24]. Specifically for PCL, Kowalski

et al. [23] reported MALDI-TOF MS (Matrix-Assisted Laser Desorption/Ionization—Time Of Flight Mass Spectrometry) evidence for Sn-containing linear and cyclic PCL macromolecules in caprolactone/$Sn(Oct)_2$ systems, supporting the assumption of covalently bound tin(II)-alkoxide polyester species formation. The reversible active/dormant species activation typical for lactide ROP is supported by the combination of MALDI-TOF end-group assignments and kinetic evidence showing reversible acid-induced deactivation of Sn-alkoxide growing chains [21]. The complementary end-group evidence comes from Libiszowski et al. [25], who used MALDI-TOF MS in a model caprolactone/$Sn(Oct)_2$/BuOH system and identified hydroxy-terminated PCL populations. They also demonstrated that the initially formed BuO(O)C–PCL–OH population evolves with time, consistent with subsequent end-group exchange/esterification processes.

While there is a relative abundance of publications dealing with experimental studies of ε-caprolactone ring opening polymerization kinetics [19, 23, 24, 26–33], publications dealing with kinetic modeling of the process are surprisingly rare. Weng et al. [34] studied copolymerization of ε-caprolactone and L,L-lactide, taking most of the kinetic parameters from the literature and at the same time estimating diffusion-controlled rate constants of propagation and transesterification from the dynamic profiles of comonomers conversion and number-average molecular weight of the produced copolymer. Rosa et al. [35] performed ε-caprolactone homopolymerization using $Sn(Oct)_2$ under fixed conditions, comparing the obtained experimental results with profiles of conversion and average molecular weight predicted for various conditions. The kinetic parameters they used were mostly taken from L,L-lactide polymerization (therefore not rigorously estimated), resulting in not really convincing agreement with experimental data. Both studies mentioned above omitted the random chain scission step, which had been previously considered for lactide ROP [36], from their assumed set of elementary reactions.

In this paper, we present our work on a multi-scale model of PCL production based on the previous one used for PLA [37]. This model consists of three sub-models (macro-, micro-, and meso-scale) and in relatively short computational time it can predict polymer microstructure and rheological properties using reaction conditions and initial concentrations of monomer, catalyst, and initiator. For the ROP production of PCL, the same types of catalyst and initiator are used as in the previous case of PLA, and we begin our study with the assumption of an equivalent reaction mechanism. However, since we consider the published kinetic models of caprolactone ring-opening polymerization to be not entirely satisfactory, we first want to verify if the previously published, experimentally validated kinetic scheme for PLA production [36, 37] can be used for PCL production modeling. Therefore, we test this hypothesis by conducting five batch polymerization experiments with altered temperature and the ratio between monomer and initiator concentrations. The experimental data are used for the rigorous estimation of kinetic parameters connected with the elementary reaction steps. Finally, analogously with our previous work on PLA, the rheological data on the produced PCL samples, which are of importance in polymer down-stream processing and final product formulation, are collected and discussed.

2 | Methodology

2.1 | Experimental

2.1.1 | Polymerization

2.1.1.1 | Materials. Benzyl alcohol (Sigma Aldrich, 99%) was used as received. Toluene (anhydrous, Honeywell, > 99%) was used as received. Tin(II) 2-ethylhexanoate (Sigma) 92.5%–100% was purified using vacuum distillation and stored in a glove box under nitrogen gas. ε-caprolactone (BLD pharmatech, 99.93%) was purified using vacuum distillation and stored in a glove box under nitrogen gas.

2.1.1.2 | Synthesis. Poly(caprolactone) synthesis was performed with simultaneous aliquot extraction for size exclusion chromatography (SEC) and ^1H NMR analysis. The general protocol goes as follows: 2 g (0.0175 mol) of caprolactone was weighed in a round-bottom flask. Seventy one milligrams of $Sn(Oct)_2$ (0.000175 mol) was weighed in a separate vial. Nineteen milligrams of benzyl alcohol (0.000175 mol) was added to a separate vial. Note that for experiments where the ratio of monomer to initiator was varied, the respective mass of benzyl alcohol was adjusted. Everything was weighed in a glovebox. A total of 4.83 mL of dry toluene was added to caprolactone, with the remaining 1 mL divided over the vials with benzyl alcohol and $Sn(Oct)_2$ for a total concentration of 3 M. Once the round-bottom flask with caprolactone has reached the desired temperature, solutions containing benzyl alcohol and $Sn(Oct)_2$ were added. After the predetermined reaction time (96 h, 54 h, 30 h), poly(caprolactone) was precipitated in cold methanol and dried in a vacuum oven at 40°C overnight.

2.1.2 | Polymer Characterization

2.1.2.1 | ^1H NMR Characterization. At various time intervals, aliquots (44 μL, ~15 mg poly(caprolactone)) were taken and left to dry. Conversion was calculated as the ratio of the monomer peak integration at 4.22 ppm and the polymer peak integration at 4.05 ppm.

2.1.2.2 | SEC Characterization. At various time intervals, aliquots (44 μL, ~15 mg poly(caprolactone)) were taken and left to dry. Measurements were performed on a TOSOH EcoSEC instrument using $CHCl_3$ eluent running at 1 mL/min. Multi-angle light scattering (MALS) ($LenS_3$, Tosoh) was used to analyze the samples. Samples were dissolved at a concentration of approximately 15 mg/mL in $CHCl_3$ with 100 ppm of toluene as an internal standard and passed through a 0.2 μm Teflon filter prior to measurement. Elugrams were converted to molar mass distributions using calibration data from polystyrene standards. Polystyrene standards (Polymer Standards Service; PSS) with a molar mass ranging from 0.4 to 1000 kg/mol were used. Raw SEC data was processed and subsequently analyzed using Igor analysis software.

Based on the results of previous studies on the kinetic mechanism of $Sn(Oct)_2$-catalyzed ROP of ε-caprolactone carried out mainly by the research group of Stanislaw Penczek (see Section 1), the existence of OH-terminated (dormant) chains in

the reaction mixture has been implicitly assumed and therefore not tested/proven by any analytical method.

2.1.2.3 | SAOS Characterization. All rheological tests were performed using a stress-controlled rotational rheometer (Anton Paar MCR 302e, Graz, Austria). The rheometer was equipped with an electrically controlled temperature hood. The analyses were conducted using a 25 mm parallel-plate geometry under a nitrogen atmosphere. All samples were characterized by frequency sweep tests using angular frequency from 0.1 to 100 rad/s at a fixed strain amplitude of 1%, within the linear viscoelastic regime. Measurement temperatures were selected based on the melting peaks identified by DSC. The temperature was carefully optimized to capture the narrow region between the rapid transition to a low-viscosity melt a few degrees above T_m (leading to low-torque limitations) and the rapid solidification of the melt upon approaching the melting point. It was not possible to analyze all the samples at the exact same temperature.

2.1.2.4 | DSC Characterization. Melting temperatures (T_m) were determined using a DSC 25 (TA Instruments, USA). For each measurement, approximately 5 mg of sample was placed in non-hermetic aluminum pans and subjected to heat–cool–heat cycles from 25°C to 200°C at a constant heating and cooling rate of 10°C/min. For each sample, T_m was determined from the second heating cycle.

2.2 | Model Description

Multi-scale modeling allows us to obtain and combine several types of information. That is why it is widely used not only in polymer science [38–40]. The scheme of our multi-scale model is depicted in Figure 1. As explained above, the structure of this model is the same as in the work of Zubov and Sin [37], who designed a multi-scale model of PLA production.

1. The first part, the macro-scale model, can be imagined as a simulation of the reactor in which the polymerization is conducted. The inputs of this model are the initial composition of the batch (i.e., concentrations of monomer, catalyst, and co-catalyst), reaction temperature, and duration of the polymerization reaction. Model results are obtained by solving material balances (under isothermal assumptions, heat balance is neglected) and population balances of polymer chains (the so-called "polymer moment" equations), resulting in a set of ordinary differential equations (ODEs). The outputs of this model are the evolution of reacting species concentrations, elementary reaction rates, monomer conversion, and number and weight-average molecular weights of polymer, M_n, and M_w, respectively.
2. The micro-scale model simulates the growth of chains using the Monte Carlo approach first published by Gillespie [41]. Its computational burden is partly lowered by utilizing the evolutions of concentrations and reaction rates computed by the previous sub-model as an input, resulting in a "hybrid" approach. This model predicts the detailed chain architecture of the produced polymer.
3. The last sub-model is a publicly available software, BoB (Branch-on-Branch) [42] model of chain reptation dynamics, allowing estimation of the rheological properties (viscous and elastic modulus, complex viscosity) based on the polymer molecular architecture provided by the Monte Carlo model.

All the sub-models are further explained in the following subsections.

2.2.1 | Macro-Scale Model

As was noted in the Introduction, in our model, we start with the same kinetic scheme as was used for the ROP of lactide by Zubov and Sin [37] and Yu et al. [36], differing only in the number of monomer units added/removed during one propagation/depropagation step, since lactide is a dimer and ε-caprolactone is a monomer. The analogous kinetic scheme is involved in this work because of the similar structure of monomers (L, L-lactide and ε-caprolactone) and the same nature of the catalyst and co-catalyst used. The assumed kinetic scheme is shown in Figure 2, where M stands for monomer unit (ε-caprolactone), C for catalyst (tin(II) octoate), and A for octanoic acid. Symbols R_n, D_n, and G_n are used for the active (growing), dormant, and terminated (dead) chains of length n, respectively. The initiator molecule can be denoted as D_0.

The kinetic parameters of propagation, transesterification, and chain scission follow the Arrhenius dependency on temperature, and are calculated using a pre-exponential factor k_{p0}, k_{te0}, k_{de0}, respectively, and activation energy, $E_{a,p}$, $E_{a,te}$, $E_{a,de}$, respectively. The activation of the catalyst is assumed fast (as in the case of

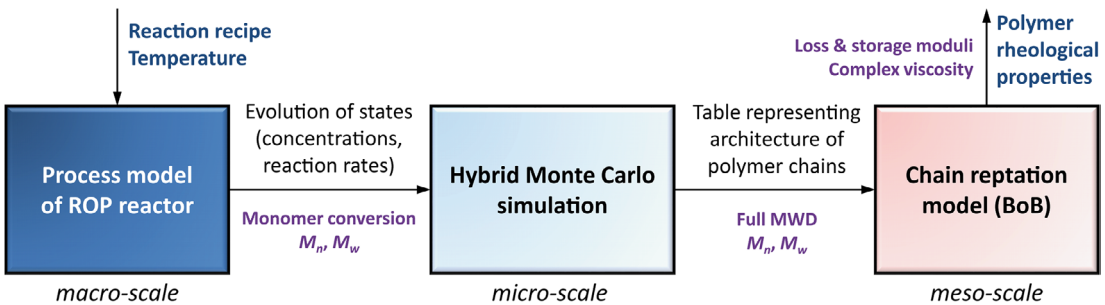

FIGURE 1 | Scheme of the multi-scale model presented in this paper. Adapted from [37] with permission given by Elsevier.

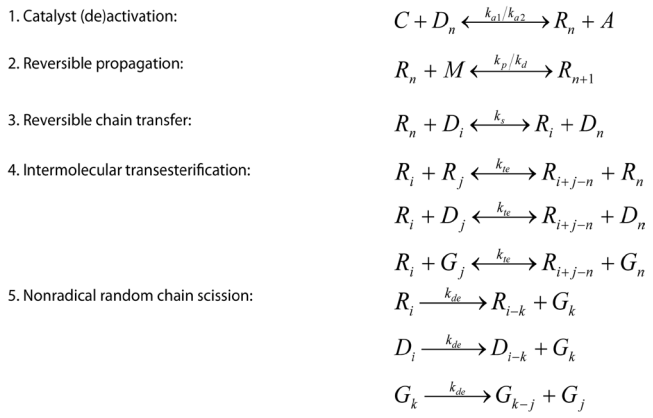

FIGURE 2 | Reaction scheme of ε-caprolactone ROP analogous to the scheme for L, L-lactide ROP presented previously in the paper by Yu et al. [36].

lactide ROP); therefore, the kinetic parameter of catalyst activation is set as constant ($k_{a1} = 10^6$ L mol^{-1} h^{-1}). The kinetic parameter of catalyst deactivation is calculated from the equilibrium constant $k_{a2} = \frac{k_{a1}}{K_{eq}}$, and the equilibrium constant is temperature dependent,

$$K_{eq} = \exp\left(-\frac{A}{T} + B\right), \tag{1}$$

with A and B being unknown parameters. The value of the depropagation rate coefficient k_d is calculated as $k_d = k_p[M_{eq}]$. The monomer equilibrium concentration $[M_{eq}]$ is dependent on temperature,

$$[M_{eq}] = \exp\left(\frac{\Delta H_{lc}}{RT} - \frac{\Delta S_{lc}}{R}\right). \tag{2}$$

where ΔH_{lc} and ΔS_{lc} are the enthalpy and entropy of polymerization, respectively.

A further description of the model can be found in the paper by Zubov and Sin [37]. Material balances of non-polymeric species and rate equations for polymer moments under the assumption of an isothermal batch reactor with constant volume of reaction mixture are presented below. In the following equations, λ_i denotes the i-th moment of the active chains' distribution, μ_i denotes the i-th moment of the dormant chains' distribution, and γ_i denotes the i-th moment of the terminated chains' distribution.

Balances of monomer, catalyst, and octoic acid:

$$\frac{dM}{dt} = -k_p M \lambda_0 + k_d \lambda_0, \tag{3}$$

$$\frac{dC}{dt} = k_{a1} C \mu_0 - k_{a2} A \lambda_0, \tag{4}$$

$$\frac{dA}{dt} = -k_{a1} C \mu_0 - k_{a2} A \lambda_0. \tag{5}$$

Moment equations for active chains:

$$\frac{d\lambda_0}{dt} = k_{a1} C \mu_0 - k_{a2} A \lambda_0, \tag{6}$$

$$\begin{aligned}\frac{d\lambda_1}{dt} = {} & k_{a1}\mu_1 C - k_{a2}\lambda_1 A + k_p M\ \lambda_0 - k_d\lambda_0 - k_s\lambda_1\mu_0 + k_s\mu_1\lambda_0 \\ & - k_{te}\lambda_1(\mu_1 - \mu_0) + \frac{1}{2}k_{te}\lambda_0(\mu_2 - \mu_1) - k_{te}\lambda_1(\gamma_1 - \gamma_0) \\ & + \frac{1}{2}k_{te}\lambda_0(\gamma_2 - \gamma_1) - \frac{1}{2}k_{de}(\lambda_2 - \lambda_1),\end{aligned} \tag{7}$$

$$\begin{aligned}\frac{d\lambda_2}{dt} = {} & k_{a1}\mu_2 C - k_{a2}\lambda_2 A + k_p M\ (2\lambda_1 + \lambda_0) + k_d(\lambda_0 - 2\lambda_1) \\ & - k_s\lambda_2\mu_0 + k_s\mu_2\lambda_0 + \frac{1}{3}k_{te}\lambda_0(\lambda_1 - \lambda_3) + k_{te}\lambda_1(\lambda_2 - \lambda_1) \\ & - k_{te}\lambda_2(\mu_1 - \mu_0) + \frac{1}{6}k_{te}\lambda_0(2\mu_3 - 3\mu_2 + \mu_1) - k_{te}\lambda_2(\gamma_1 - \gamma_0) \\ & + \frac{1}{6}k_{te}\lambda_0(2\gamma_3 - 3\gamma_2 + \gamma_1) - \frac{1}{6}k_{de}(4\lambda_3 - 3\lambda_2 - \lambda_1).\end{aligned} \tag{8}$$

Moment equations for dormant chains:

$$\frac{d\mu_0}{dt} = -k_{a1}\mu_0 C + k_{a2}\lambda_0 A, \tag{9}$$

$$\begin{aligned}\frac{d\mu_1}{dt} = {} & -k_{a1}\mu_1 C + k_{a2}\lambda_1 A + k_s\lambda_1\mu_0 - k_s\mu_1\lambda_0 + k_{te}\lambda_1(\mu_1 - \mu_0) \\ & - \frac{1}{2}k_{te}\lambda_0(\mu_2 - \mu_1) - \frac{1}{2}k_{de}(\mu_2 - \mu_1),\end{aligned} \tag{10}$$

$$\begin{aligned}\frac{d\mu_2}{dt} = {} & -k_{a1}\mu_2 C + k_{a2}\lambda_2 A + k_s\lambda_2\mu_0 - k_s\mu_2\lambda_0. \\ & + k_{te}\lambda_2(\mu_1 - \mu_0) + k_{te}\lambda_1(\mu_2 - \mu_1) \\ & + 1/6\,k_{te}\lambda_0(-4\mu_3 + 3\mu_2 + \mu_1) \\ & - 1/6\,k_{de}(4\mu_3 - 3\mu_2 - \mu_1).\end{aligned} \tag{11}$$

Moment equations for terminated chains:

$$\frac{d\gamma_0}{dt} = k_{de}(\lambda_1 - \lambda_0) + k_{de}(\mu_1 - \mu_0), \tag{12}$$

$$\begin{aligned}\frac{d\gamma_1}{dt} = {} & k_{te}\lambda_1(\gamma_1 - \gamma_0) - \frac{1}{2}k_{te}\lambda_0(\gamma_2 - \gamma_1) - k_{de}(\gamma_2 - \gamma_1) \\ & + \frac{1}{2}k_{de}(\lambda_2 - \lambda_1) + \frac{1}{2}k_{de}(\mu_2 - \mu_1),\end{aligned} \tag{13}$$

$$\begin{aligned}\frac{d\gamma_2}{dt} = {} & k_{te}\lambda_2(\gamma_1 - \gamma_0) + k_{te}\lambda_1(\gamma_2 - \gamma_1) + \frac{1}{6}k_{te}\lambda_0(-4\gamma_3 + 3\gamma_2 + \gamma_1) \\ & - \frac{1}{3}k_{de}(4\gamma_3 - 3\gamma_2 - \gamma_1) + \frac{1}{6}k_{de}(2\lambda_3 - 3\lambda_2 + \lambda_1) \\ & + \frac{1}{6}k_{de}(2\mu_3 - 3\mu_2 + \mu_1).\end{aligned} \tag{14}$$

All the third order moments are calculated from the following closure formulas:

$$\lambda_3 = \frac{\lambda_2(2\lambda_2\lambda_0 - \lambda_1^2)}{(\lambda_1\lambda_0)}, \tag{15}$$

$$\mu_3 = \frac{\mu_2\left(2\mu_2\mu_0 - \mu_1^2\right)}{\left(\mu_1\mu_0\right)}, \tag{16}$$

$$\gamma_3 = \frac{\gamma_2\left(2\gamma_2\gamma_0 - \gamma_1^2\right)}{\left(\gamma_1\gamma_0\right)}. \tag{17}$$

2.2.2 | Micro-Scale Model

The Monte Carlo model is based on a stochastic simulation algorithm for dynamic modeling of coupled reactions [41]. We have used the same implementation of this algorithm as Zubov and Sin [37], where it is described in detail. The main difference that must be implemented is represented by the different number of monomer units in one monomer molecule, which was mentioned above (two for PLA and one for PCL).

At the beginning of the Monte Carlo simulation, initial concentrations are converted to "micro-scale" units in terms of finite numbers (amounts) of simulated "particles," so that the reaction rates R_i of each elementary reaction step have physical units of reciprocal time. During the simulation, the probability p_i of the i-th reaction is calculated from its reaction rate (R_i) in the current time step,

$$p_i = \frac{R_i}{\sum_{j=1}^{M} R_j}. \tag{18}$$

Using the pseudorandom number generator, one of the reactions is selected, and the set of simulated "particles" is modified accordingly. After that, the simulation time is increased by Δt,

$$\Delta t = \frac{\ln r_2}{\sum_{j=1}^{M} R_j}, \tag{19}$$

where r_2 is a pseudo-random number from a uniformly distributed interval [0, 1].

As mentioned at the beginning of Section 2.2, to improve simulation performance, the reaction rates for the micro-scale model are pre-computed using the concentration profiles predicted by the macro-scale model.

2.2.3 | Meso-Scale Model

The last sub-model is based on the Branch-on-Branch algorithm to predict the rheological properties of the polymer melt at a chosen temperature. This model is publicly available as a precompiled executable file [42]. This model needs the following input: polymer architecture or mean molecular weights (only for linear polymers), temperature at which the rheological properties should be predicted, molecular weight of monomer unit, polymer melt density, mean chain entanglement length, and characteristic entanglement time. The last two parameters characterize the interactions between the chains (entanglements) and need to be estimated. Further description of how the model is incorporated into the multi-scale scheme, including global sensitivity analysis of its input model parameters, can be found in the paper by Zubov and Sin [37].

2.3 | Estimation of Kinetic Parameters

Similar to Zubov and Sin [37], we assume that the kinetic rate coefficients of catalyst activation and chain transfer are constant. To decrease the size of the optimization problem, we have used values of ΔH_{lc} and ΔS_{lc} found in literature [43]. Therefore, we had to estimate the values of eight parameters: constants of catalyst activation/deactivation equilibrium A and B (Equation 1), pre-exponential factor of propagation k_{p0}, and activation energy of propagation $E_{a,p}$ pre-exponential factor and activation energy of intermolecular transesterification k_{te0} and $E_{a,te}$, and pre-exponential factor and activation energy of non-radical chain scission k_{de0} and $E_{a,de}$. This is done via nonlinear regression utilizing experimental data describing the dynamic evolution of caprolactone conversion (X), polymer number- and weight-average molecular weight over time (M_n, M_w).

For the estimation of kinetic parameters, we have re-implemented the macro-scale model in MATLAB. MATLAB was chosen because of an efficient optimization algorithm based on Differential Evolution [44]. In both parts of the optimization problem, the objective function was constructed as the sum of squares of differences between N measured experimental values and the results of model predictions at the same points in time.

$$\mathrm{SSR} = \sum_{i=1}^{N}\left(X^{\mathrm{exp}} - X^{\mathrm{sim}}\right)^2 + \sum_{i=1}^{N}\left(M_n^{\mathrm{exp}} - M_n^{\mathrm{sim}}\right)^2 + \sum_{i=1}^{N}\left(M_w^{\mathrm{exp}} - M_w^{\mathrm{sim}}\right)^2, \tag{20}$$

where *SSR* is the squared sum of residuals, superscript *exp* denotes experimental results, and superscript *sim* denotes results from the mathematical model. Since conversion of monomer X is assumed between 0% and 100%, the relative magnitude of its term is quantitatively comparable to that of polymer molar mass terms (in kg/mol); therefore, no weights for the individual terms of the squared residuals sum have been used.

After a few attempts to find the absolute values of all parameters, we have decided to do pre-optimization and find the order of magnitude of pre-exponential factors. The upper and lower bounds used during pre-optimization are presented in Table S1. Using the pre-optimization results, the bounds for final optimization were defined, see Table S2.

2.4 | Uncertainty Analysis

In this work, the same approach as described in the paper by Ruszczyński et al. [25] was used to evaluate the 95% confidence intervals of the estimated kinetic parameters. We utilized the *nlparci* function, implemented in MATLAB [45]. Using the Jacobian matrix and vector of residuals precomputed with the MATLAB algorithm lsqnonlin, it first calculates the covariance matrix as follows:

$$\mathrm{COV}(\theta) = \frac{\mathrm{resv}}{n}\left(J(\theta)^T \cdot J(\theta)\right)^{-1}, \tag{21}$$

where COV(x) is the covariance matrix, *resv* is the residual vector, $J(x)$ Jacobian matrix, and n are degrees of freedom, which

TABLE 1 | Table of parameter values for the proposed kinetic scheme with 95% confidence intervals for optimized parameters.

Parameter	Value	Standard deviation	Source
k_{a1}	$1\times10^{6}\,\mathrm{L\,mol^{-1}\,h^{-1}}$	—	Assumed
A (K_{eq} par.)	$-2.93\times10^{4}\,\mathrm{K}$	2.34%	Estimated
B (K_{eq} par.)	85.51	2.38%	Estimated
k_{p0}	$3.33\times10^{6}\,\mathrm{L\,mol^{-1}\,h^{-1}}$	13.18%	Estimated
$E_{a,p}$	$38.84\,\mathrm{kJ\,mol^{-1}}$	1.24%	Estimated
ΔH_{lc}	$-28.8\,\mathrm{kJ\,mol^{-1}}$	—	[43]
ΔS_{lc}	$-53.9\,\mathrm{J\,mol^{-1}\,K^{-1}}$	—	[43]
k_{s}	$1\times10^{6}\,\mathrm{L\,mol^{-1}\,h^{-1}}$	—	Assumed
k_{te0}	$6.86\times10^{5}\,\mathrm{L\,mol^{-1}\,h^{-1}}$	9.78%	Estimated
$E_{a,te}$	$50.00\,\mathrm{kJ\,mol^{-1}}$	2.85%	Estimated
k_{de0}	$2.73\times10^{7}\,\mathrm{h^{-1}}$	18.19%	Estimated
$E_{a,de}$	$79.10\,\mathrm{kJ\,mol^{-1}}$	0.86%	Estimated

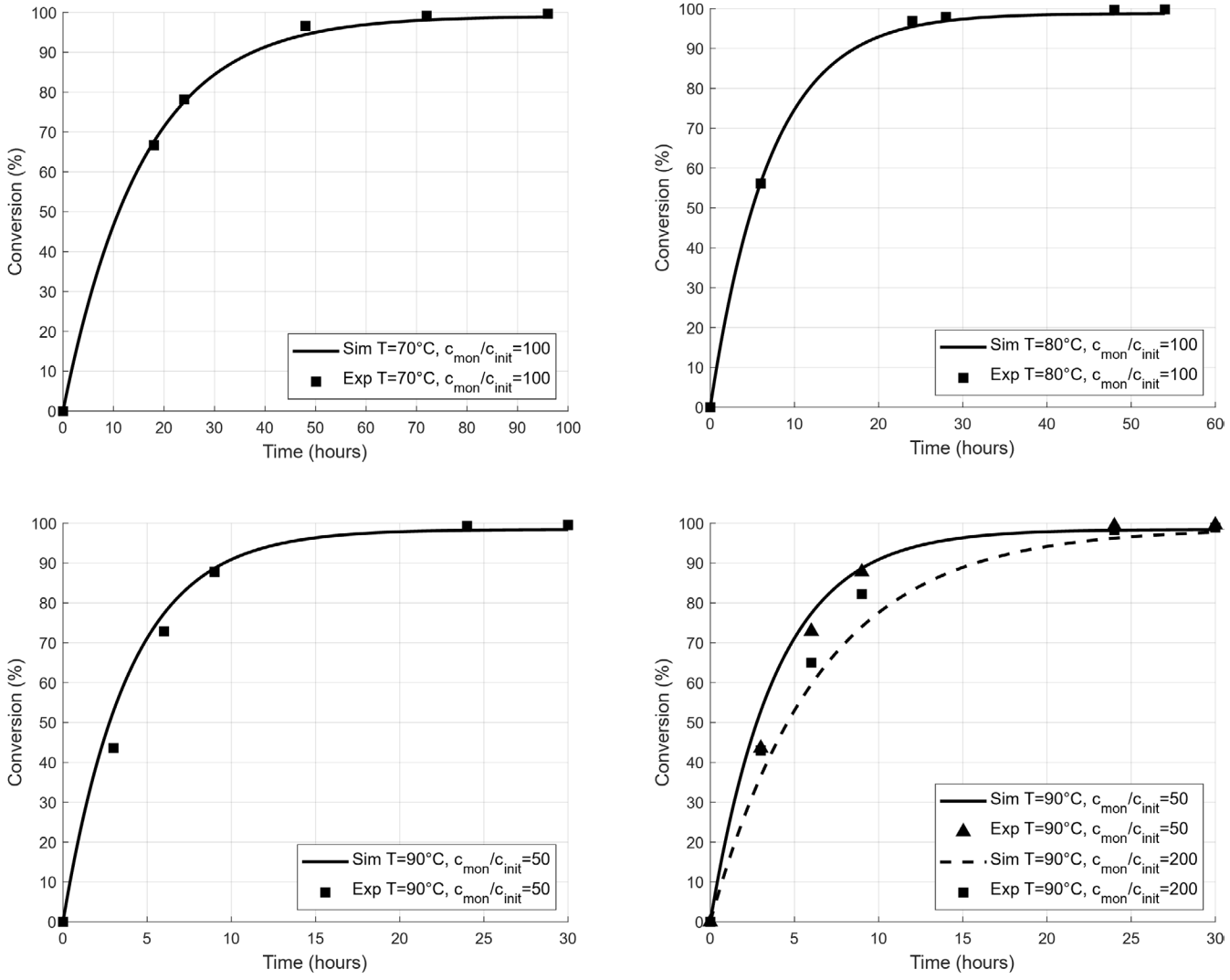

FIGURE 3 | Plots of monomer (ε-caprolactone) conversion temporal evolution at various reaction temperatures and monomer/initiator ratios, estimated experimentally (discrete points) and compared with macro-scale model predictions (curves).

are defined as $n = n_{resv}, -n_p$, where n_{resv} is the length of the residual vector and n_p is the number of parameters. The confidence interval at an α significance level is computed as

$$\theta_{1-\alpha} = \theta \pm \sqrt{\text{diag}(\text{COV}(\theta))} \cdot t\left(n, \frac{\alpha}{2}\right), \tag{22}$$

where $t\left(n, \frac{\alpha}{2}\right)$ is the value of the t-distribution at $\alpha/2$ percentile with n degrees of freedom.

3 | Results and Discussion

3.1 | Estimated Kinetic Parameters

The optimization of *SSR* was conducted as described in Section 2.3. As a result, we have obtained the searched values of parameters describing the kinetics of the studied ROP. Standard deviations of these values were estimated using the algorithm described in Section 2.4. Values of all parameters and their standard deviations are listed in Table 1.

The values of standard deviations were relatively low for most of the parameters. The highest values are observed for the pre-exponential factors. This can be expected since it was difficult to find the order of magnitude, and optimization was divided into two steps, as described in Section 2.3.

3.2 | Polymerization Kinetics

The results of the macro-scale model simulation with optimized parameters were compared with the experimental results. In Figure 3, experimental and simulated results of monomer conversion in time at different temperatures and with different ratios of monomer and initiator are compared. Let us note that the error bars (standard deviation) could not be estimated for the experimental data, because the polymer synthesis runs have not been replicated. This was mainly due to their time-consuming nature (i.e., experiments lasting up to 100 h). Nevertheless, we find this approach to be quite typical for the polymerization modeling studies in general [34–36].

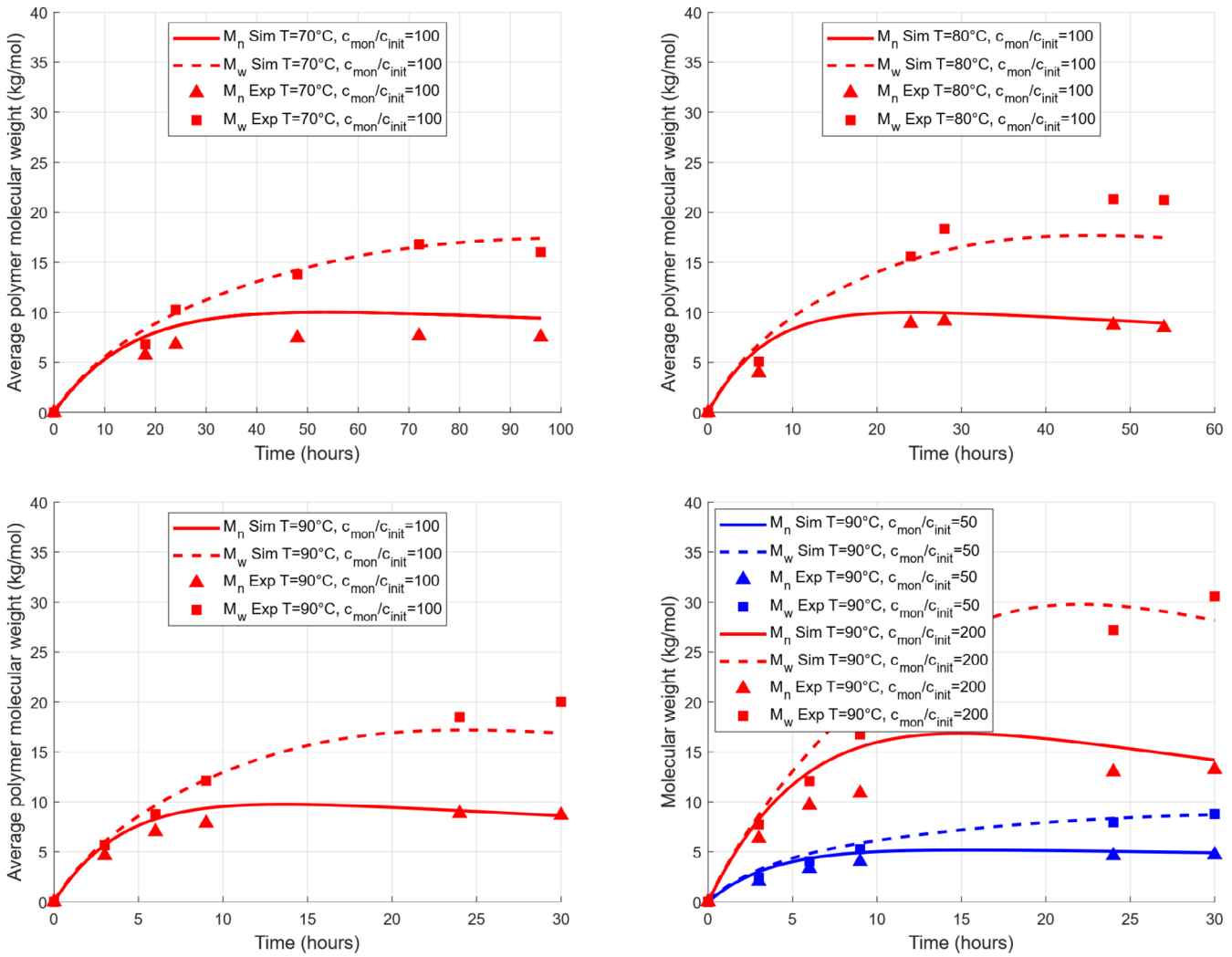

FIGURE 4 | Plots of number and weight-average polymer molecular weights M_n, M_w, temporal evolution during ε-caprolactone ROP evaluated experimentally (discrete points) and compared with macro-scale model predictions (curves) at various reaction temperatures and monomer/initiator ratios.

As it is noticeable, the agreement between experimental and model results is exceptionally good. When compared with PLA production, for which analogous kinetic scheme has been experimentally validated [36], we observe significantly slower dynamics of polymerization here: at 80°C, propagation rate coefficient of PCL is $k_{p,\mathrm{PCL}} = 5.99$ L/mol/h, while for PLA it is $k_{p,\mathrm{PLA}} = 320.7$ L/mol/h. In Figure 4, the polymer average molar masses M_n and M_w predicted by the macro-scale model and estimated experimentally are compared. We can observe decent agreement between experimental and modeling results, but it is noticeable that at later stages of polymerization, after 30 h, when conversion of monomer reaches almost 100%, the deviation between experimental and predicted values is slightly higher, especially in case of weight-average molecular weight M_w. The evolution of polymer molar mass, when almost all monomer molecules have been depleted, is caused by chain "reshuffling" reactions, which are represented by intermolecular transesterification in our assumed kinetic scheme.

Overall, we can conclude that the trends predicted by the macro-scale (population balance) model render well the observed experimental data. Therefore, the kinetic scheme previously proposed for ring-opening polymerization of L,L-lactide, which includes reversible catalyst activation, reversible propagation, reversible chain transfer, reversible intermolecular transesterification, and nonradical chain scission, can be successfully applied in the context of PCL production as well. Values of final properties (M_n and PDI) of the samples studied are listed together with the reaction conditions in Table 2.

3.3 | Micro-Scale (Monte Carlo) Model Validation

First, we have verified that the micro-scale model is predicting the same evolutions of the molecular weight distribution moments as the macro-scale model. For this purpose, it is necessary to calculate polymer molar weight averages M_n^{MC} and M_w^{MC} from the macromolecular microstructure predicted by the Monte Carlo algorithm.

$$M_n^{MC} = M_M \frac{\sum_{i=1}^{N_R} R_{MC}(i) + \sum_{j=1}^{N_D} D_{MC}(j) + \sum_{k=1}^{N_G} G_{MC}(k)}{N_R + N_D + N_G}, \tag{23}$$

$$M_w^{MC} = M_M \frac{\sum_{i=1}^{N_R} R_{MC}(i)^2 + \sum_{j=1}^{N_D} D_{MC}(j)^2 + \sum_{k=1}^{N_G} G_{MC}(k)^2}{\sum_{i=1}^{N_R} R_{MC}(i) + \sum_{j=1}^{N_D} D_{MC}(j) + \sum_{k=1}^{N_G} G_{MC}(k)}, \tag{24}$$

TABLE 2 | Final properties of all samples listed together with reaction conditions.

	Reaction temperature (°C)	Monomer/initiator ratio (–)	M_n (g mol^{-1})	PDI (–)
Sample 1	70	100	7521.8	2.1
Sample 2	80	100	8457.8	2.5
Sample 3	90	100	8674.6	2.3
Sample 4	90	50	4702.6	1.8
Sample 5	90	200	13240.2	2.2

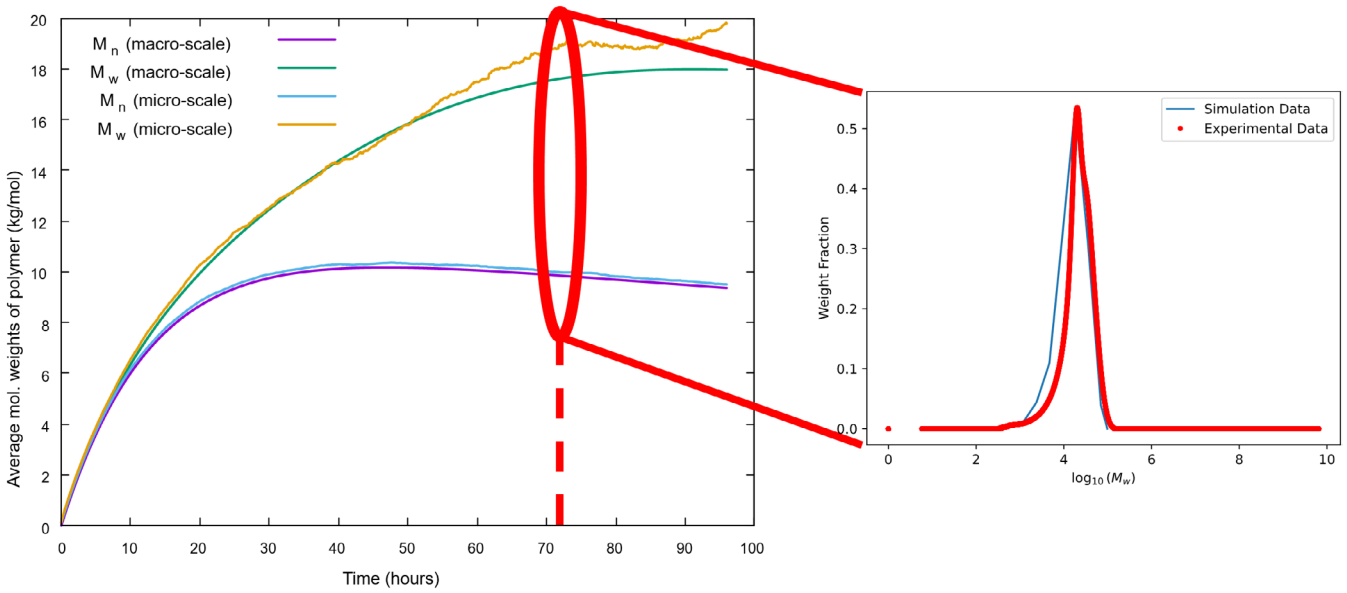

FIGURE 5 | Comparison of M_n and M_w predicted by macro-scale and micro-scale models (on the left) and comparison of GPC curve measured after 72 h of polymerization and distribution of molecular weights predicted by the micro-scale model at the same reaction time. The polymerization was conducted for 96 h at 70°C, and the ratio of monomer and initiator concentrations was 100.

where M_M is the molecular weight of monomer, N_R, N_D, N_G stand for the total number of active, dormant, and terminated chains, respectively, and R_{MC}, D_{MC}, G_{MC} represent vectors of simulated active, dormant, and terminated chain lengths, respectively. The comparison of the results of these two submodels simulating ROP at 70°C with a monomer/initiator concentration ratio of 100 for 96 h is shown in Figure 5. The curves produced by these two models overlap for most of the period. In the times after 50 h, the oscillations of M_w evolution predicted by the micro-scale model are more pronounced.

The primary outcome of the micro-scale model is the complete distribution of chain lengths or molecular weights. These distributions in chosen times were compared with experimentally measured gel permeation chromatography (GPC) data. One of these comparisons (taken specifically at 72 h of polymerization) is shown in Figure 5. Based on this comparison, we can notice that the hybrid Monte Carlo (micro-scale) model is able to quantitatively predict the shape of the GPC curve/molar weights distribution.

3.4 | Rheological Characteristics of Produced PCL

The linear viscoelastic behavior of four synthesized PCL samples (in the state of melt) was experimentally characterized using small amplitude oscillatory shear (SAOS) measurements. Figure 6 presents the dependence of storage modulus (G') and loss modulus (G'') on the frequency of oscillations (ω). The samples span number-average molecular weights M_n between 4.7 and 13.2 kg/mol with polydispersities ranging from 1.9 to 2.5.

For all investigated samples, the loss modulus exceeds the storage modulus across the accessible frequency window (0.1–100 rad/s), and no G'–G'' crossover is observed. Moreover, storage modulus G' does not display a well-developed ω^2 terminal scaling over an extended frequency decade. These features indicate that the materials reside in a weakly entangled or transitional regime rather than in the fully developed reptation regime of long-chain polymer melts. For PCL, the critical molecular weight (M_c) is reported to be approximately

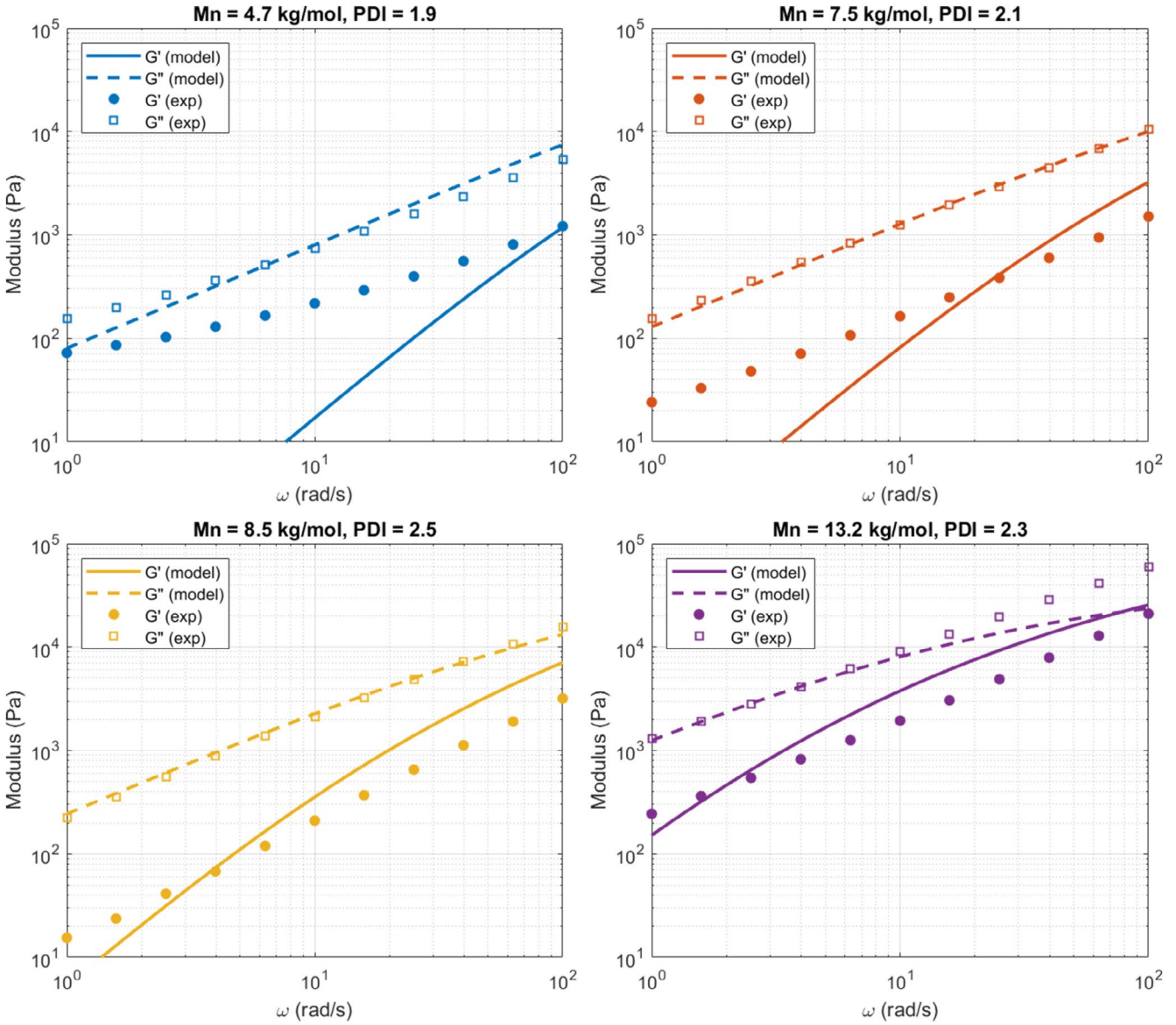

FIGURE 6 | Frequency sweep characteristics of the four synthesized PCL samples. Comparison of experimental (points) and predicted (curves) values of storage (G') and loss (G'') moduli in dependence on the frequency of oscillations.

6 kg/mol [46, 47]. The samples prepared in this work exhibit weight-average molecular weights M_w between 8.8 and 30 kg/mol, corresponding to M_w/M_c ratios roughly between 1.5 and 5, respectively. Consequently, the samples are characterized by rather low entanglement regime ($M_w/M_c < 5$) [46], in which the relaxation spectrum is governed by a crossover between Rouse-like segmental dynamics and emerging reptation constraints, and classical terminal behavior is not yet fully developed [48, 49].

The absence of a crossover point and the lack of a well-developed rubbery plateau indicate that the samples do not reside in the fully entangled reptation regime. Classical tube-based models, including architecture-resolved implementations such as the Branch-on-Branch (BoB) algorithm, which is part of our modeling framework, rely on the existence of a well-defined entanglement network characterized by a plateau modulus and reptation-dominated terminal relaxation. In the present low molecular weight regime, such models are outside their formal range of validity [42]. Consequently, a different, simplified mathematical description based directly on the polymer molecular weight distribution was attempted to model the measured rheological response of the PCL samples.

The linear viscoelastic response was calculated based on measured polymer molecular weight distributions using Maxwell superposition [50, 51] over discretized molecular weight fractions and is presented in Figure 6 as continuous curves. For each fraction of molecular weight M, the relaxation time $\tau(M)$ was assigned according to a crossover scaling:

$$\tau \propto M^2 \text{ for } M < M_e \text{ (Rouse regime)},$$

$$\tau \propto M^3 \text{ for } M \geq M_e \text{ (weakly entangled regime)},$$

with $M_e = M_c/2 = 3$ kg/mol and continuity imposed at $M = M_e$. This approach follows the classical framework of polymer dynamics [48, 49] and provides a physically meaningful bridge between unentangled and weakly entangled behavior. A single input parameter τ_c (estimated to be on the order of 10^{-6} s) was used to position the relaxation spectrum at the measurement temperature. No additional fitting parameters were introduced.

The reconstructed loss modulus spectra exhibit relatively good agreement with experimental G'' data across all four samples, particularly in the intermediate frequency range. The model correctly reproduces the systematic increase in dissipative response with molecular weight, demonstrating that the predicted molecular weight distributions are consistent with the observed relaxation dynamics. In contrast, systematic deviations are observed in the storage modulus at low frequencies, where the experimental G' decreases more slowly than predicted by the homogeneous melt model. Such behavior is indicative of an additional slow elastic contribution not captured by the linear molecular-weight-based framework. In semicrystalline polyesters such as PCL, possible origins include weak microstructural heterogeneities or residual low-molecular-weight species. These effects can introduce a solid-like component that elevates G' without significantly altering the mid-frequency dissipative response.

Overall, the modeling results confirm that the primary rheological trends are governed by molecular weight and distribution characteristics predicted by the polymerization model, while secondary deviations can be attributed to physical phenomena beyond the scope of an ideal homogeneous melt description.

4 | Conclusions and Future Work

In this paper, we have described a multi-scale model of PCL production via ring-opening polymerization (ROP) of ε-caprolactone. The model is based on the previously published multi-scale model of L,L-lactide ROP. We have built upon the analogy between these two processes and proposed a similar kinetic mechanism of polymerization.

Five batch polymerization experiments with varying temperature and ratio of monomer and initiator were conducted, leading to the production of linear PCL samples of varying molecular weight distributions. During these experiments, evolutions of monomer conversion were estimated using NMR, and molecular weight distribution moments were estimated using the combination of NMR and GPC. These data were used to estimate the complete set of necessary parameters describing the kinetics of ε-caprolactone ROP, including their standard deviations. Comparison of the model predictions with experimental data reveals that although the polymerization dynamics are significantly slower for ROP of ε-caprolactone than for L,L-lactide, the original kinetic scheme previously validated for PLA production can be successfully used to model the PCL production process. Similarly to the PLA production, the intermolecular transesterification, resulting in a random "reshuffling" of polymer chain segments, leads to the increase of product polydispersity at the advanced stages of polymerization. In contrast to the previous modeling studies [34, 35], our results indicate that in caprolactone/Sn(Oct)$_2$ ROP, random chain scission might play a role already at temperatures around 80°C.

Due to the relatively low molecular weight of the produced PCL samples, which results in a transitional, not fully entangled regime, the rheological prediction originally proposed in our modeling framework (tube theory-based software "BoB") could not be used. The linear viscoelastic response could be partially reconstructed using Maxwell superposition based on the molecular weight distribution of the samples.

The future work in this area will involve modeling of nonlinear ring-opening polymerization based on poly-functional alcohols, leading to polymer chain branching. With the whole multi-scale modeling framework going from reaction recipe to the product melt rheology developed and experimentally validated, the design of PCL-based biodegradable materials with tailored viscoelastic properties can be accelerated.

Acknowledgments

This work was supported from the grant of Specific university research—grant no A1_FCHI_2026_005. Partial financial support from Hasselt University under the project Bijzonder Onderzoeksfond (BOF) R-12788 (BOF22K04) is greatly appreciated. Open access publishing

facilitated by Vysoka skola chemicko-technologicka v Praze, as part of the Wiley - CzechELib agreement.

Funding

This work was supported by Universiteit Hasselt under the project Bijzonder Onderzoeksfond, R-12788 (BOF22K04), and by Vysoká Škola Chemicko-technologická v Praze (UCT Prague), Specific university research grant A1_FCHI_2026_005.

Data Availability Statement

The data that support the findings of this study are available from the corresponding author upon reasonable request.

References

1. X. X. Deng, M. Gould, and M. A. Ali, "Fabrication and Characterisation of Melt-Extruded Chitosan/Keratin/PCL/PEG Drug-Eluting Sutures Designed for Wound Healing," *Materials Science & Engineering, C: Materials for Biological Applications* 120 (2021): 111696, https://doi.org/10.1016/j.msec.2020.111696.

2. J. A. Grotting, T. J. Nelson, M. B. Banffy, et al., "Biomechanical Evaluation of PCL Reconstruction With Suture Augmentation," *Knee* 27, no. 2 (2020): 375–383, https://doi.org/10.1016/j.knee.2020.01.004.

3. S. M. Eskitoros-Togay, "Investigation of Effects of Modified Montmorillonite-Doped Electrospun Nanofibers on Drug Delivery Systems," *Journal of Polymer Science* 63, no. 8 (2025): 1808–1823, https://doi.org/10.1002/pol.20241018.

4. Z. Zhang, H. Sun, J. Giannino, Y. Wu, and C. Cheng, "Biodegradable Zwitterionic Polymers as PEG Alternatives for Drug Delivery," *Journal of Polymer Science* 62, no. 10 (2024): 2231–2250, https://doi.org/10.1002/pol.20230916.

5. M. M. Rovers, J. E. P. Brouns, F. W. B. Craenmehr, et al., "Controlling Drug Release From Supramolecular Polymer Surfaces by a Click-To-Release Reaction," *Journal of Polymer Science* 63, no. 14 (2025): 2934–2943, https://doi.org/10.1002/pol.20250133.

6. M. V. S. Pereira, G. G. Fonseca, T. A. Andrade, et al., "Amphiphilic Nanocarrier Based on Poly(ε-Caprolactone) for Biomimetic Membrane Permeation and Controlled Lithium Delivery: An In Vitro Study," *Journal of Polymer Science* 63, no. 22 (2025): 4869–4879, https://doi.org/10.1002/pol.20250541.

7. Q. S. Dong, M. Zhang, X. X. Zhou, et al., "3D-Printed Mg-Incorporated PCL-Based Scaffolds: A Promising Approach for Bone Healing," *Materials Science & Engineering, C: Materials for Biological Applications* 129 (2021): 112372, https://doi.org/10.1016/j.msec.2021.112372.

8. M. L. Yang, W. Y. Sun, L. Wang, et al., "Curcumin Loaded Polycaprolactone Scaffold Capable of Anti-Inflammation to Enhance Tracheal Cartilage Regeneration," *Materials & Design* 224 (2022): 111299, https://doi.org/10.1016/j.matdes.2022.111299.

9. N. Siddiqui, S. Asawa, B. Birru, R. Baadhe, and S. Rao, "PCL-Based Composite Scaffold Matrices for Tissue Engineering Applications," *Molecular Biotechnology* 60, no. 7 (2018): 506–532, https://doi.org/10.1007/s12033-018-0084-5.

10. S. Park, M. S. Lee, J. Jeon, et al., "Micro-Groove Patterned PCL Patches With DOPA for Rat Achilles Tendon Regeneration," *Journal of Industrial and Engineering Chemistry* 105 (2022): 352–364, https://doi.org/10.1016/j.jiec.2021.09.037.

11. L. Yang, X. F. Li, D. M. Wang, et al., "Improved Mechanical Properties by Modifying Fibrin Scaffold With PCL and Its Biocompatibility Evaluation," *Journal of Biomaterials Science, Polymer Edition* 31, no. 5 (2020): 658–678, https://doi.org/10.1080/09205063.2019.1710370.

12. W. Pi, L. P. Zhou, W. Zhang, et al., "Three-Dimensional Conductive Polycaprolactone/Carbon Nanotubes Scaffolds for Peripheral Nerve Regeneration," *Journal of Materials Science* 57, no. 24 (2022): 11289–11299, https://doi.org/10.1007/s10853-022-07336-z.

13. M. Amini and A. M. Bittner, "Novel 3D-Printed PCL/CMC Scaffolds for Enhanced Bone Regeneration," *Journal of Polymer Science* 63, no. 19 (2025): 3944–3956, https://doi.org/10.1002/pol.20250265.

14. S. Behtaj, F. Karamali, E. Masaeli, Y. G. Anissimov, and M. Rybachuk, "Electrospun PGS/PCL, PLLA/PCL, PLGA/PCL and Pure PCL Scaffolds for Retinal Progenitor Cell Cultivation," *Biochemical Engineering Journal* 166 (2021): 107846, https://doi.org/10.1016/j.bej.2020.107846.

15. E. Pintos, C. Sarmoria, A. Brandolin, and M. Asteasuain, "Modeling of RAFT Polymerization Processes Using an Efficient Monte Carlo Algorithm in Julia," *Industrial & Engineering Chemistry Research* 55, no. 31 (2016): 8534–8547, https://doi.org/10.1021/acs.iecr.6b01639.

16. A. Zubov, J. Pokorny, and J. Kosek, "Styrene–Butadiene Rubber (SBR) Production by Emulsion Polymerization: Dynamic Modeling and Intensification of the Process," *Chemical Engineering Journal* 207–208 (2012): 414–420, https://doi.org/10.1016/j.cej.2012.06.144.

17. M. A. Woodruff and D. W. Hutmacher, "The Return of a Forgotten Polymer-Polycaprolactone in the 21st Century," *Progress in Polymer Science* 35, no. 10 (2010): 1217–1256, https://doi.org/10.1016/j.progpolymsci.2010.04.002.

18. G. Rafler and J. Dahlmann, "Biodegradable Polymers. 6th Comm. Polymerization of ε-Caprolactone," *Acta Polymerica* 43, no. 2 (1992): 91–95, https://doi.org/10.1002/actp.1992.010430207.

19. D. Wu, Y. Lv, R. Guo, et al., "Kinetics of Sn(Oct)(2)-Catalyzed Ring Opening Polymerization of Epsilon-Caprolactone," *Macromolecular Research* 25, no. 11 (2017): 1070–1075, https://doi.org/10.1007/s13233-017-5148-z.

20. A. Kowalski, J. Libiszowski, T. Biela, M. Cypryk, A. Duda, and S. Penczek, "Kinetics and Mechanism of Cyclic Esters Polymerization Initiated With Tin(II) Octoate. Polymerization of ε-Caprolactone and L,L-Lactide Co-Initiated With Primary Amines," *Macromolecules* 38, no. 20 (2005): 8170–8176, https://doi.org/10.1021/ma050752j.

21. A. Kowalski, A. Duda, and S. Penczek, "Kinetics and Mechanism of Cyclic Esters Polymerization Initiated With Tin(II) Octoate, 1 Polymerization of ε-Caprolactone," *Macromolecular Rapid Communications* 19, no. 11 (1998): 567–572, https://doi.org/10.1002/(SICI)1521-3927(19981101)19:11<567::AID-MARC567>3.3.CO;2-K.

22. A. Kowalski, A. Duda, and S. Penczek, "Kinetics and Mechanism of Cyclic Esters Polymerization Initiated With Tin(II) Octoate. 3. Polymerization of L,L-Dilactide," *Macromolecules* 33, no. 20 (2000): 7359–7370, https://doi.org/10.1021/ma000125o.

23. A. Kowalski, A. Duda, and S. Penczek, "Mechanism of Cyclic Ester Polymerization Initiated With Tin(II) Octoate. 2. Macromolecules Fitted With Tin(II) Alkoxide Species Observed Directly in MALDI-TOF Spectra," *Macromolecules* 33, no. 3 (2000): 689–695, https://doi.org/10.1021/ma9906940.

24. R. F. Storey and J. W. Sherman, "Kinetics and Mechanism of the Stannous Octoate-Catalyzed Bulk Polymerization of ε-Caprolactone," *Macromolecules* 35, no. 5 (2002): 1504–1512, https://doi.org/10.1021/ma010986c.

25. J. Libiszowski, A. Kowalski, A. E. Duda, and S. Penczek, "Kinetics and Mechanism of Cyclic Esters Polymerization Initiated With Covalent Metal Carboxylates, 5 -: End-Group Studies in the Model ε-Caprolactone and L,L-Dilactide/Tin(II) and Zinc Octoate/Butyl Alcohol Systems," *Macromolecular Chemistry and Physics* 203, no. 10–11 (2002): 1694–1701, https://doi.org/10.1002/1521-3935(200207)203:10/11<1694::AID-MACP1694>3.0.CO;2-J.

26. W.-D. Fu, J. Jiang, Y. Zhang, J. J. Li, L. Zhao, and Z. Xi, "Kinetic Modeling of Cationic Ring-Opening Polymerization for the Synthesis of

Biodegradable Poly(ε-Caprolactone)," *Chemical Engineering Science* 290 (2024): 119876, https://doi.org/10.1016/j.ces.2024.119876.

27. M. A. F. Delgove, A. A. Wróblewska, J. Stouten, et al., "Organocatalyzed Ring Opening Polymerization of Regio-Isomeric Lactones: Reactivity and Thermodynamics Considerations," *Polymer Chemistry* 11, no. 21 (2020): 3573–3584, https://doi.org/10.1039/C9PY01777A.

28. Y. Liu, L. Song, N. Feng, et al., "Recent Advances in the Synthesis of Biodegradable Polyesters by Sustainable Polymerization: Lipase-Catalyzed Polymerization," *RSC Advances* 10, no. 59 (2020): 36230–36240, https://doi.org/10.1039/D0RA07138B.

29. F. Naz, F. Mumtaz, S. Chaemchuen, and F. Verpoort, "Bulk Ring-Opening Polymerization of ε-Caprolactone by Zeolitic Imidazolate Framework," *Catalysis Letters* 149, no. 8 (2019): 2132–2141, https://doi.org/10.1007/s10562-019-02816-5.

30. C. Sattayanon, N. Kungwan, W. Punyodom, P. Meepowpan, and S. Jungsuttiwong, "Theoretical Investigation on the Mechanism and Kinetics of the Ring-Opening Polymerization of ε-Caprolactone Initiated by Tin(II) Alkoxides," *Journal of Molecular Modeling* 19, no. 12 (2013): 5377–5385, https://doi.org/10.1007/s00894-013-2026-2.

31. W. A. Munzeiwa, B. O. Omondi, and V. O. Nyamori, "A Perspective Into Ring-Opening Polymerization of ε-Caprolactone and Lactides: Effect of, Ligand, Catalyst Structure and System Dynamics, on Catalytic Activity and Polymer Properties," *Polymer Bulletin* 81, no. 11 (2024): 9419–9464, https://doi.org/10.1007/s00289-024-05149-5.

32. W. Limwanich, W. Meelua, P. Meepowpan, and W. Punyodom, "Kinetics and Thermodynamics Studies of the Ring-Opening Polymerization of ε-Caprolactone Initiated by Titanium(IV) Alkoxides by Isothermal Differential Scanning Calorimetry," *Reaction Kinetics, Mechanisms and Catalysis* 135, no. 2 (2022): 881–895, https://doi.org/10.1007/s11144-022-02184-z.

33. K. Kaluzynski, P. Lewinski, J. Pretula, R. Szymanski, and S. Penczek, "ε-Caprolactone Polymerization Catalyzed by Heteropolyacid. Derivation of the Kinetic Equation for Activated Monomer Propagation and Determination of the Rate Constants of Propagation," *Macromolecules* 52, no. 17 (2019): 6405–6415, https://doi.org/10.1021/acs.macromol.9b00672.

34. F. Y. Weng, X. H. Li, Y. J. Wang, W. J. Wang, and S. J. Severtson, "Kinetics and Modeling of Ring-Opening Copolymerization of L-Lactide and ε-Caprolactone," *Macromolecular Reaction Engineering* 9, no. 6 (2015): 535–544, https://doi.org/10.1002/mren.201500009.

35. R. P. Rosa, F. V. Ferreira, A. P. K. Saravia, et al., "A Combined Computational and Experimental Study on the Polymerization of Epsilon-Caprolactone," *Industrial & Engineering Chemistry Research* 57, no. 40 (2018): 13387–13395, https://doi.org/10.1021/acs.iecr.8b03288.

36. Y. C. Yu, G. Storti, and M. Morbidelli, "Kinetics of Ring-Opening Polymerization of L,L-Lactide," *Industrial & Engineering Chemistry Research* 50, no. 13 (2011): 7927–7940, https://doi.org/10.1021/ie200117n.

37. A. Zubov and G. Sin, "Multiscale Modeling of Poly(Lactic Acid) Production: From Reaction Conditions to Rheology of Polymer Melt," *Chemical Engineering Journal* 336 (2018): 361–375, https://doi.org/10.1016/j.cej.2017.12.033.

38. K. Kulajanpeng, N. Sheibat-Othman, W. Tanthapanichakoon, and T. F. L. McKenna, "Multiscale Modelling of Multizone Gas Phase Propylene (Co)polymerization Reactors-A Comprehensive Review," *Canadian Journal of Chemical Engineering* 100, no. 9 (2022): 2505–2545, https://doi.org/10.1002/cjce.24471.

39. A. K. Thakur, S. K. Gupta, and P. Chaudhari, "Slurry-Phase Ethylene Polymerization Processes: A Review on Multiscale Modeling and Simulations," *Reviews in Chemical Engineering* 38, no. 5 (2022): 539–568, https://doi.org/10.1515/revce-2020-0048.

40. F. Dabbagh, S. Pirker, and S. Schneiderbauer, "A Fast Modeling of Chemical Reactions in Industrial-Scale Olefin Polymerization Fluidized Beds Using Recurrence CFD," *AICHE Journal* 67, no. 5 (2021): e17161, https://doi.org/10.1002/aic.17161.

41. D. T. Gillespie, "A General Method for Numerically Simulating the Stochastic Time Evolution of Coupled Chemical Reactions," *Journal of Computational Physics* 22, no. 4 (1976): 403–434, https://doi.org/10.1016/0021-9991(76)90041-3.

42. C. Das, N. J. Inkson, D. J. Read, M. A. Kelmanson, and T. C. B. McLeish, "Computational Linear Rheology of General Branch-On-Branch Polymers," *Journal of Rheology* 50, no. 2 (2006): 207–234, https://doi.org/10.1122/1.2167487.

43. A. Duda and A. Kowalski, "Thermodynamics and Kinetics of Ring-Opening Polymerization," in *Handbook of Ring-Opening Polymerization* (Wiley, 2009), 1–51.

44. K. Price, R. Storn, and J. Lampinen, *Differential Evolution-A Practical Approach to Global Optimization* (Springer, 2005).

45. G. A. F. Seber and C. J. Wild, *Nonlinear Regression*, 1st ed. (Wiley, 1989).

46. J. Gimenez, P. Cassagnau, and A. Michel, "Bulk Polymerization of ε-Caprolactone: Rheological Predictive Laws," *Journal of Rheology* 44, no. 3 (2000): 527–547, https://doi.org/10.1122/1.551099.

47. L. Sangroniz, F. Barbieri, D. Cavallo, et al., "Rheology of Self-Nucleated Poly(c-Caprolactone) Melts," *European Polymer Journal* 99 (2018): 495–503, https://doi.org/10.1016/j.eurpolymj.2018.01.009.

48. M. Doi, S. F. Edwards, and S. F. Edwards, *The Theory of Polymer Dynamics* (Clarendon Press, 1988).

49. M. Rubinstein and R. H. Colby, *Polymer Physics* (Oxford University Press, 2003).

50. J. D. Ferry and H. S. Myers, "Viscoelastic Properties of Polymers," *Journal of the Electrochemical Society* 108, no. 7 (1961): 142C–143C.

51. M. Baumgaertel, A. Schausberger, and H. H. Winter, "The Relaxation of Polymers With Linear Flexible Chains of Uniform Length," *Rheologica Acta* 29, no. 5 (1990): 400–408, https://doi.org/10.1007/BF01376790.

Supporting Information

Additional supporting information can be found online in the Supporting Information section. **Table S1:** List of upper and lower bounds for the pre-optimization. **Table S2:** Upper and lower bounds for the optimization problem, finding values of kinetic parameters for the proposed reaction mechanism.